Time-dependent defect spectroscopy for characterization of border traps in metal-oxide-semiconductor transistors

Tibor Grasser*
Christian Doppler Laboratory for TCAD at the Institute for Microelectronics, Gußhausstraße 27-29, A-1040 Wien, Austria

Hans Reisinger
Infineon Technologies AG, Munich, Germany

Paul-Jürgen Wagner
Christian Doppler Laboratory for TCAD at the Institute for Microelectronics, Gußhausstraße 27-29, A-1040 Wien, Austria

Ben Kaczer
IMEC, Kapeldreef 75, B-3001 Leuven, Belgium
(Received 21 April 2010; revised manuscript received 15 November 2010; published 17 December 2010)

We introduce the time-dependent defect spectroscopy (TDDS) for the analysis of a particular class of oxide defects known as "border traps." These defects have a fundamental impact on the behavior of metal-oxide-semiconductor field-effect transistors and are commonly linked to the occurrence of random-telegraph noise, $1/f$ noise, and slow charging transients. The TDDS naturally extends the successful *deep-level transient spectroscopy* as it extracts both the capture and emission time constants. Analysis proceeds via the so-called *spectral maps*, which separate individual border traps by their characteristic times and their voltage step height. In contrast to standard random-telegraph noise analysis methods, where uncorrelated capture and emission events of only a few traps can already create convoluted noise patterns, the synchronization by the charging pulse yields the *spectral maps*, which allow for the analysis of a large number of defect occupancies in a single measurement. As a consequence, the TDDS allows us to monitor the defect parameters over exceptionally wide temperature and bias ranges.

DOI: 10.1103/PhysRevB.82.245318 PACS number(s): 72.20.Jv, 73.40.Qv, 73.20.Hb, 71.55.Ak

I. INTRODUCTION

Defects at the semiconductor-insulator interface as well as inside the insulator result in nonideal behavior of metal-oxide-semiconductor field-effect transistors (MOSFETs). Since the detailed microscopic nature of these defects is still controversial, a phenomenological classification into interface traps (fast states), border states (slow states, anomalous positive charge), and oxide traps (fixed oxide charge, etc.) is often employed.[1,2] The fast interface states are commonly attributed to P_{b0} and P_{b1} centers, which are trivalent silicon dangling bonds at the SiO_2/Si interface.[3] Charge exchange between interface states and the substrate appears to be consistent with the theory suggested by Shockley, Read, and Hall (SRH).[4]

In contrast, border states are still not fully understood.[5–8] They are commonly considered the cause of random telegraph and $1/f$ noise[6] as well as slow charging and discharging transients causing threshold voltage shifts in the bias temperature instability (BTI).[9–13] Similarly to interface states, these border states also communicate with the inversion layer in the channel by exchanging charge carriers, albeit on longer time scales. Microscopically, border states are often associated with E' centers (trivalent silicon dangling bonds in the oxide)[3,14] but have also been related to hydrogenic defects.[15,16]

These border states impact the operation of MOSFETs by causing random fluctuations in the terminal currents. The fluctuations are due to defects randomly exchanging charge with the substrate.[5,17] As the number of defects in a transistor follow a Poisson distribution, with the mean scaling with the device area,[18] discrete levels can be observed in small-area devices. This form of noise has become known as random-telegraph noise (RTN).[5,17]

Irrespective of the physical mechanism invoked to describe the actual capture and emission process, the defect occupancy f_t is conventionally described by a Markov process with two states. The transition probabilities between these states are exponentially distributed[5,19,20] with average capture and emission time constants $\bar{\tau}_e$ and $\bar{\tau}_c$. These time constant can be extracted by analyzing the statistics of the RTN. Best results are obtained when the defect has time constants well within the typical experimental window (milliseconds to minutes) and of about the same magnitude (mark-space ratio of about one, that is, $\bar{\tau}_e/\bar{\tau}_c \sim 1$).

Individual defects are commonly identified by the characteristic step heights they introduce in either the drain current or the threshold voltage: due to the inhomogeneous potential inside the channel caused by the randomly placed dopants,[21] the current flowing from source to drain is inhomogeneous. Depending on the relative position of the defect to the dopants, each defect will induce a different change in the drain current when its charge state is changed. The resulting step height can be considerably larger than the value obtained from the charge-sheet approximation.[22] Such steps are commonly referred to as "giant" steps in RTN literature[5,12,21] and indicate that the defect lies right above a so-called current percolation path.[23]

 ©2010 The American Physical Society

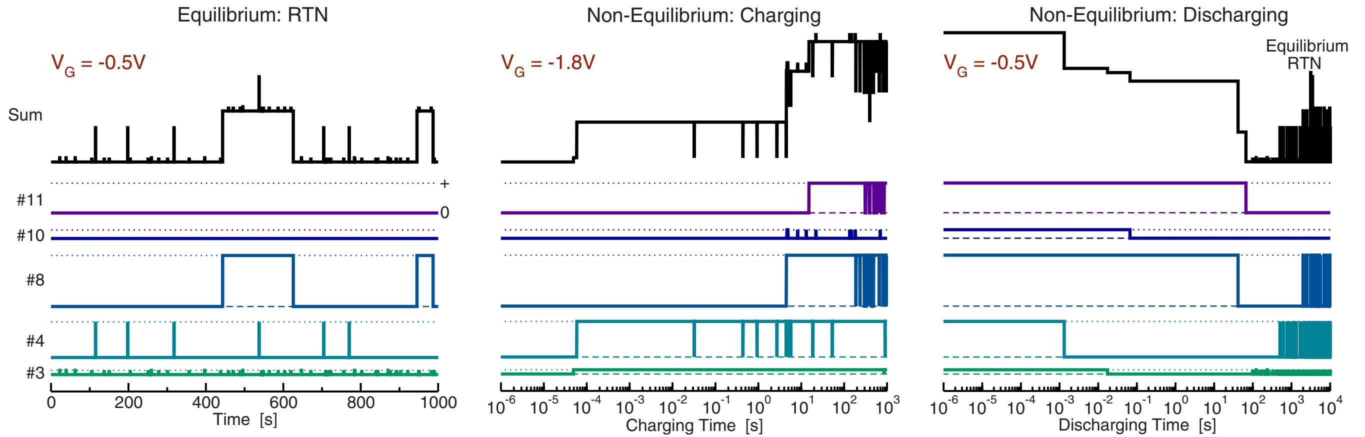

FIG. 1. (Color online) Comparison of charge capture and emission events during RTN analysis (left) with the synchronized capture and emission events during the TDDS (middle and right). For clarity, only five of the thirteen defects of the example pMOS studied in this paper are used. Their stochastic behavior was simulated using real parameters extracted by the TDDS at 175 °C. Left: close to the threshold voltage (V_G=−0.5 V), the RTN is dominated by defect #3 with the occasional contribution from defects #4 and #8. Defects #10 and #11 have larger time constants (400 ks and 1.5 Ms) and remain neutral within the experimental window. Middle: application of the charging voltage (V_G=−1.8 V) results in a nonequilibrium response of the defects which are assumed to be initially discharged. Due to the strong field-dependence of $\bar{\tau}_c$, the defects become predominantly positively charged. For larger charging times ($t_s \gtrsim \bar{\tau}_c$), the RTN produced by each defect is visible on the logarithmic scale. Right: following the perturbing charging step, defects with $\bar{\tau}_c \lesssim t_s$ are likely to be synchronized in their charged states. A switch back to a lower voltage again results in a nonequilibrium response until equilibrium is reached after the longest decorrelation time due to defect #11. Each discrete step in the transient is due to the emission of a single hole, following its emission time constant. At the end of the recovery trace, equilibrium RTN is observed again.

A crucial limitation is given by the fact that a multitude of defects can contribute to this RTN, thereby obscuring the activity of individual defects. This is schematically illustrated in the left panel of Fig. 1. It can be clearly seen how the trapping and detrapping of holes in the three defects #3, #4, and #8 sum up to a more complicated RTN. At this bias condition, defects #10 and #11 have capture times well outside any reasonable measurement window and thus do not contribute to the RTN. On average, most defects are not occupied by a hole and thus electrically neutral.

When the number of active defects is increased, for instance, at higher gate biases or temperatures, the RTN becomes increasingly difficult to analyze.[24] As a consequence, the bias and temperature dependencies of a single defect are very difficult to monitor over a wider range since sooner or later another defect will start to become active. Then, interesting features in the defect behavior may be missed.

The typical challenges inherent to the RTN analysis method can be thus summarized: (i) analysis of complex RTN signals due to multiple defects is difficult because of the random and uncorrelated capture and emission events. This makes it difficult to even estimate the number of defects contributing to the signal, let alone the bias and voltage dependencies of their capture and emission times.[24–26] (ii) The bias and temperature ranges, where only a single defect is active, are relatively small while the defect may show interesting properties outside this window. (iii) Defects with a mark-space ratio of about one dominate RTN while most defects can be expected to have widely different capture and emission times. Thus, only a limited subset of defects can be efficiently monitored using this technique.

In contrast to conventional RTN analysis, which monitors the superposition of a number of uncorrelated stationary stochastic processes in *equilibrium*, techniques such as the deep-level transient spectroscopy (DLTS) (Refs. 27 and 28) perturb the system to analyze the equilibration of the defects. Of particular interest is the application of the DLTS to small-area transistors, where the transients proceed in discrete steps, reminiscent of RTN.[20] Each step is due to charge exchange between a single defect and the channel, a phenomenon which has been successfully used to extract the emission times of individual defects. The perturbation is caused by switching between charging and discharging bias conditions, which, due to the strong-bias dependence of the time constants, results in charging and discharging transients, see the middle and right panels of Fig. 1. During these transients, whose lengths are on the order of the asymptotic decorrelation time,[29] $(1/\bar{\tau}_c + 1/\bar{\tau}_e)^{-1}$, each defect approaches its new equilibrium.

Although the small-area DLTS appears to be very powerful, its potential has not been fully exploited as of yet, possibly due to difficulties encountered during the manual analysis of the discrete steps. In fact, only a single paper[20] reports on its application. In the following we will suggest an extension of the small-area DLTS method which we term *time-dependent defect spectroscopy* (TDDS). A new name is introduced because of the different analysis of the accumulated data: (i) a frequently employed assumption in the DLTS is that all defects are charged after a filling pulse of a certain duration.[20] This assumption is incorrect as the capture time constant shows a very wide distribution, a fact observed as a nonsaturating behavior in the DLTS spectra.[30] (ii) In order to simultaneously analyze the discrete steps caused by the discharging of a dozen of defects, the TDDS introduces *spectral maps*, which visualize the emission events separated by emission times and voltage step heights. (iii) A spectral map

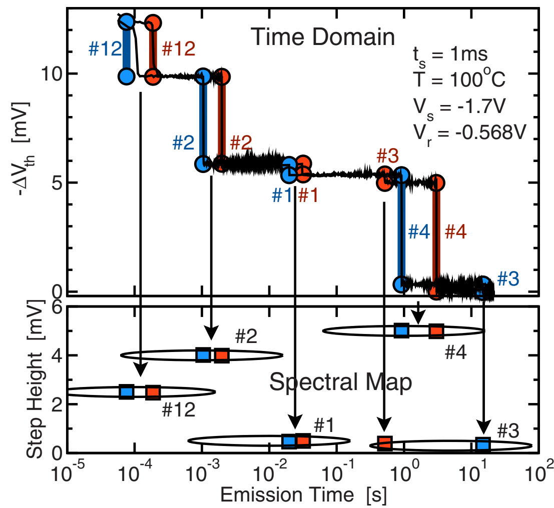

FIG. 2. (Color online) Two typical threshold-voltage recovery traces of a pMOSFET. The measured data are given by the (slightly noisy) thin black lines in the top part of the figure. The thick blue and red lines together with the symbols mark the automatically extracted emission times and step heights which are nearly unambiguous fingerprints of each defect and build the spectral map (bottom).

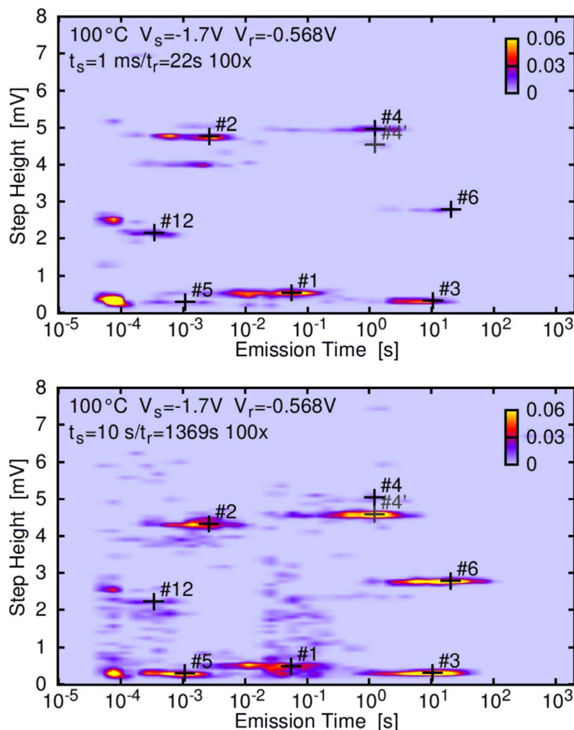

FIG. 3. (Color online) Spectral maps obtained after two different stress times, $t_s=1$ ms (top) and $t_s=10$ s (bottom). The parameters are given in the top-left corner of each map (Line 1: temperature, stress/charging voltage, recovery/discharging voltage. Line 2: stress time, recovery time, number of traces). With increasing stress time, the number of defects contributing to the map increases since defects with $\bar{\tau}_c \lesssim t_s$ have a significant probability of being positively charged after stress. Note that only #1, #3, and #5 have amplitudes close to what is expected from the charge-sheet approximation (0.9 mV).

is recorded using a fixed charging time. Additional spectral maps are recorded with increasing charging times, which results in more and more defects appearing on the maps. This allows for the calculation of the capture time constant.

Most RTN studies so far have been performed on n-channel devices and considered electron capture. Because of the technological relevance of hole capture in the oxide of p-channel devices, as, for instance, observed during negative bias temperature stress,[8,10,13,31–33] the versatility of the TDDS and the plethora of observable defects will be demonstrated on a single, selected, production-quality p-channel MOSFET (Ref. 34) with a 2.2-nm-thick plasma-nitrided oxide and $W/L=150$ nm/100 nm. In that particular device we are able to monitor the average capture and emission time constants of 13 defects as a function of bias (gate and drain) as well as temperature.

After introducing the TDDS, we demonstrate its versatility by highlighting as-of-yet unappreciated intricacies related to this hole-capture process. In particular, our data suggest that no defect follows a simple two-state Markov process due to the existence and importance of metastable defect states.

II. TIME-DEPENDENT DEFECT SPECTROSCOPY

The basic TDDS setup is as follows: after a charging period at a higher gate voltage, the gate voltage is switched to a lower discharging voltage during which the subsequent charge-emission transient is recorded. The charging/discharging sequence is repeated N times until accurate statistics can be gathered. Since the TDDS can cover not only the whole operation regime of the transistor but also charging voltages commonly encountered in accelerated reliability tests,[31] we refer to the charging pulse as the stress pulse and the charge emission transient as the recovery transient.

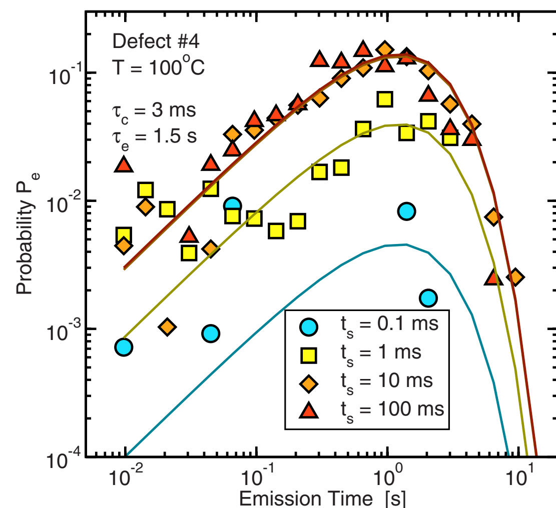

FIG. 4. (Color online) Extraction of the emission time constant for defect #4 using a 1D histogram, where all events with $4<d<6$ mV are plotted as a function of the emission time. The data is shown for four different stress times. At each stress time, the data (symbols) can be described by $P_c P_e$ (lines). For $t_s \geq 10$ ms, P_c equals 1, that is, the number of emission events does not change anymore with increasing stress time.

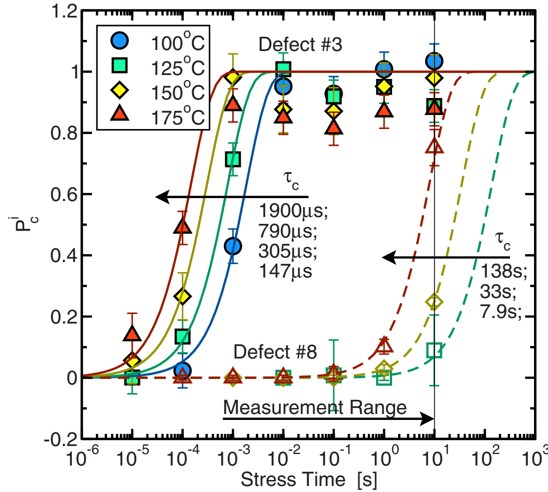

FIG. 5. (Color online) Example extraction of the capture time constant at four different temperatures. With increasing stress time and temperature the number of defects contributing to the map increases. This makes the identification of the discrete steps more difficult and the noise level in the maps increases. Consequently, the clusters become wider, resulting in a spurious decrease in $P_c^{(i)}$, which may show a visible deviation from unity even for $t_s \gg \bar{\tau}_c$.

In the pMOS transistor used in our study we only observed hole capture into neutral defects, resulting in a negative shift of the threshold voltage. The discharging transient is recorded starting from the microsecond regime using the previously developed ultrafast technique, which employs the feedback loop of an operational amplifier.[34] It monitors the change in the threshold voltage of the transistor, ΔV_{th}, which is determined as the change in V_G at constant I_D. Alternatively, the change in I_D at constant V_G may be recorded.[20,35] Knowledge of ΔV_{th}, however, allows comparison of the extracted step heights with the "reference value" obtained from the charge-sheet approximation.

After a charging/stress pulse of duration t_s, the defects present in the device will emit their charges as a function of the recovery time t_r according to

$$-\Delta V_{th}(t_s,t_r) = \sum_i d^{(i)} H(t_s - \tau_c^{(i)}) H(\tau_e^{(i)} - t_r), \qquad (1)$$

with the Heaviside function $H(t)$, the characteristic step height $d^{(i)}$, and the capture and emission times $\tau_c^{(i)}$ and $\tau_e^{(i)}$ of defect i, respectively. As the example device is a pMOSFET were a negative threshold voltage shift is observed, we analyze $-\Delta V_{th}$ in order to obtain positive step heights $d^{(i)}$. Note that while both stochastic variables $\tau_c^{(i)}$ and $\tau_e^{(i)}$ are a function of the gate bias, $\tau_c^{(i)}$ depends on the stress voltage $V_G = V_s$ while $\tau_e^{(i)}$ is recorded at the recovery (or readout) voltage $V_G = V_r$. The capture and emission time constants are the expectation values of the capture and emission times, that is, $\bar{\tau}_e^{(i)} = \mathrm{E}\{\tau_e^{(i)}\}$ and $\bar{\tau}_c^{(i)} = \mathrm{E}\{\tau_c^{(i)}\}$.

In the initial analysis step, the measured recovery traces are approximated by Eq. (1) using a straightforward curve tracing algorithm. Emission events are characterized by their emission time and step height, $(\tau_e^{(i)}, d^{(i)})$, which are then binned into a two-dimensional (2D) histogram, see Fig. 2. The entries in the 2D histogram are then normalized by N to obtain the spectral map after the stress time t_s. In Eq. (1) the recapture of charge during one transient is ignored, which is normally the case when $\bar{\tau}_c(V_r) \gg \bar{\tau}_e(V_r)$. The latter can be experimentally assured by selecting devices which do not show appreciable RTN at $V_G = V_r$.

According to the Markov model, the capture and emission times are exponentially distributed.[5,19] Thus, the probability of $\tau_e^{(i)}$ falling into bin j is given by

$$P_e^{(i,j)} = \exp(-\tau^{(j)}/\bar{\tau}_e^{(i)}) - \exp(-\tau^{(j+1)}/\bar{\tau}_e^{(i)}), \qquad (2)$$

where the $\tau^{(j+1)} = \lambda \tau^{(j)}$ are the boundaries of the bins in τ direction and i denotes the defect.

The spectral maps do not only allow for the extraction of $\bar{\tau}_e$ and the step height d but also for the capture time constant $\bar{\tau}_c$. Naturally, determination of $\bar{\tau}_c$ is only possible for defects visible on the spectral map. However, defects with $\bar{\tau}_c$ much smaller than the stress time can be expected to appear with a 100% probability on the spectral map. This provides no information on $\bar{\tau}_c$. On the other hand, defects with capture times much larger than the stress time will not appear at all. In the intermediate regime, however, where the capture time is on the order of the stress time, the number of hits per cluster will increase exponentially, allowing for an accurate determination of $\bar{\tau}_c$. Provided $\bar{\tau}_c^{(i)}(V_s) \ll \bar{\tau}_e^{(i)}(V_s)$ we have

$$P_c^{(i)} = 1 - \exp(-t_s/\bar{\tau}_c^{(i)}). \qquad (3)$$

Thus, M spectral maps with increasing stress time are recorded to also extract the capture time constant of the defects appearing on the maps. One map per decade in time-proved

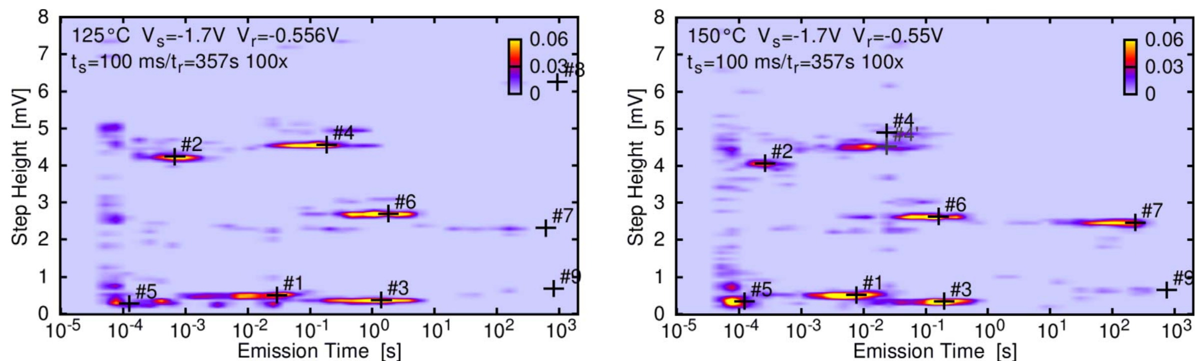

FIG. 6. (Color online) Temperature dependence of the spectral maps after $t_s = 100$ ms. With increasing temperature, the emission times decrease. As also the capture time constants decreases, the clusters appear after a shorter stress time.

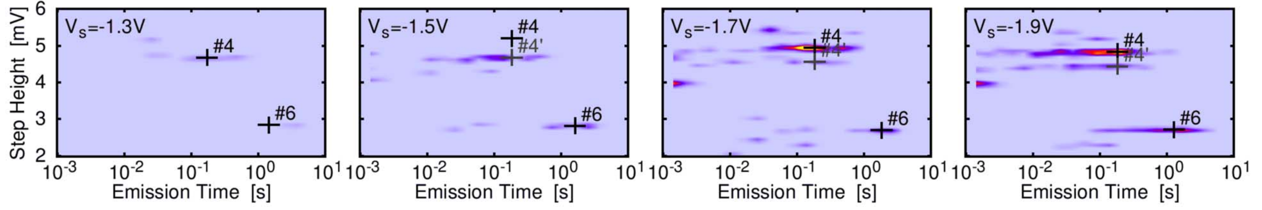

FIG. 7. (Color online) Partial spectral maps showing the stress bias dependence at $T=125$ °C and $t_s=1$ ms. With increasing stress voltage the intensity of the clusters increases. In addition, the step height of #4 splits into two peaks due to the electrostatic interaction with #6.

sufficiently accurate and we used stress times $t_s \in \{1\ \mu s, 10\ \mu s, \ldots, 10\ s\}$. The overall effect of using M maps is that the defects are not only deconvoluted according to their emission times and step heights as on a single map but also according to their capture times. Thus, provided that a defect has either a different emission time, a different step height, or a different capture time compared to any other defect, it can be clearly identified. This is the reason for the unique accuracy of the TDDS. We now proceed by demonstrating the versatility of the TDDS using a number of example cases.

III. STANDARD DEFECT BEHAVIOR

We begin our discussion with cases, where the defect behavior is apparently compatible with a two-state Markov process. Two example spectral maps for $V_s=-1.7$ V, $V_r=V_{th}$, and $T=100$ °C but different t_s are shown in Fig. 3. As expected from theory, marked clusters of (τ_e, d) pairs evolve, the intensity (number of events/number of traces) of which typically follows P_c.

For demonstration purposes, the result of a simpler analysis based on one-dimensional (1D) histograms is shown in Fig. 4. This particular 1D histogram is an integrated version of the 2D spectral map over the step height in the window $4<d<6$ mV. The probability of having an emission event with $\tau_e \in [\tau^{(j)}, \tau^{(j+1)}]$ is given by $P_c P_e$, which nicely agrees with the experimental data as demonstrated in Fig. 4.

In Fig. 5 the extraction of $\bar{\tau}_c$, for defects #3 and #8 is shown based on the P_c extracted from the spectral maps. Defect #3 has about the same step height as #1 (≈ 0.4 mV) while their emission time constants are separated by a factor of about 500 at 100 °C, which decreases to 10 at 175 °C. At 100 °C, this separation is reasonably large due to the different activation energies (see Fig. 3) and $P_c^{(3)}(t_s)$ approaches unity, as expected from $P_c(t_s \gg \bar{\tau}_c)$. Since the activation energy of $\bar{\tau}_e$ of #3 is about twice as large as that of #1 (cf. Fig. 6), the emission events related to #1 and #3 increasingly overlap with increasing temperature, making the extraction of both $P_c^{(1)}(t_s)$ and $P_c^{(3)}(t_s)$ more difficult. This is visible as a marked deviation of $P_c^{(3)}(t_s)$ from unity in Fig. 5. Alternatively, the deviation from unity can be a consequence of defect metastability, as discussed in Sec. IV. Another interesting case given in Fig. 5 is #8, which has a capture time constant larger than the largest stress time used in our experiments.

At higher temperatures, the clusters appear with shorter emission times, see Fig. 6. This confirms that we are dealing with a thermally activated emission process.[5] Also, all clusters appear already after shorter stress times, demonstrating the thermally activated nature of charge capture. For example, after a 100 ms stress the cluster corresponding to defect #7 is already fully developed at 150 °C while it only gradually begins to form at 125 °C.

The bias dependence of the capture time constant can be clearly observed in the partial maps shown in Fig. 7. Keeping t_s fixed at 1 ms, the number of emission events per cluster increases with increasing stress bias, demonstrating the strong-bias dependence of $\bar{\tau}_c$.

Closer inspection of Fig. 3, for instance, of defects #4 and #6, reveal that the step height is subject to slight variations, depending on the most dominant current conduction path[21] which can change with the occurrence of additional charged defects. This effect is only visible in the 2D spectral maps. Mostly, the peaks show similar emission times, however, significant differences in the emission times have also been observed. The correlation analysis in Fig. 8 clearly shows that the emission events marked as #4 and #4′, respectively, #6 and #6′ are due to the same defects, because even after stress times much larger than the capture time constant, nearly perfect anticorrelation of the subpeaks is observed.

Another confirmation of the fact that the electrically detected step height is a consequence of the interaction of the defect charge with the random potential in the channel is given in Fig. 9. Just like in RTN, the step height is highly

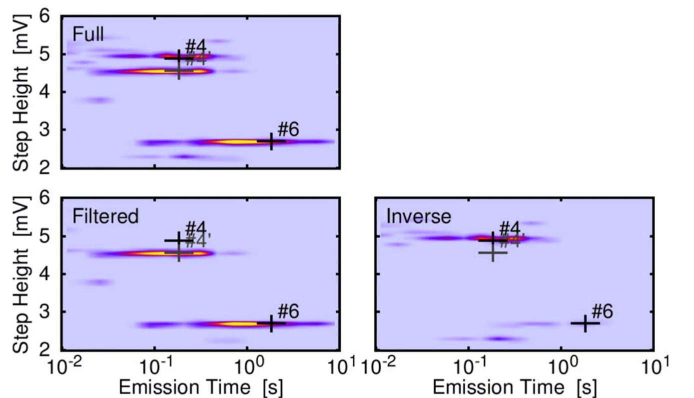

FIG. 8. (Color online) Quite regularly, a single defect produces peaks of different height in the maps. For instance, #4 appears as #4 and #4′ (top). Filtering out all traces that produce an event in #4′ (top) reveals that as soon as #6 is occupied, #4 produces an event in the #4 cluster. Otherwise, for an unoccupied #6, an event in the #4′ cluster is obtained (bottom).

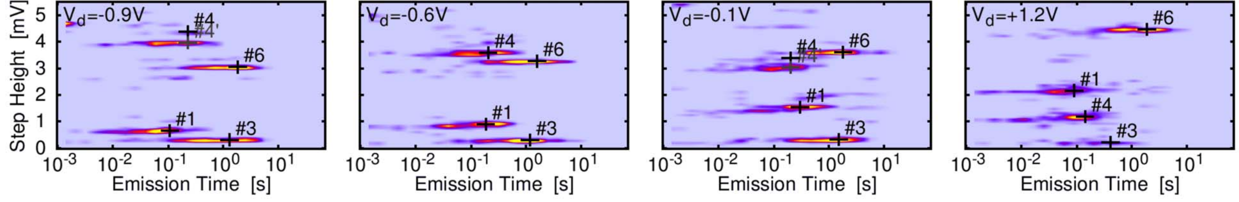

FIG. 9. (Color online) Partial spectral maps showing the drain bias sensitivity of the defect parameters at $T=125$ °C, $V_s=-1.5$ V, and $t_s=100$ ms. For instance, when the drain bias is changed from −0.9 V to −0.6 V, −0.1 V and eventually "+1.2 V" (symbolic for source and drain reversed), the step height of #1 increases from 0.8 to 2.1 mV, #4 decreases from 4 to 1 mV, and #6 increases from 3 to 4.3 mV. Note that even though defects #1, #4, and #6 dramatically change their relative positions, reliable extraction of the defect parameters remains possible.

sensitive to the drain bias used during readout. Figure 9 clearly shows how the defects can change place in the spectral map depending on the drain bias. We consider it a particular strength of the TDDS that the defect parameters can be reliably extracted even in these cases.

Of particular, practical relevance is the recovery gate bias dependence of the emission times since a strong-bias dependence could be used to efficiently remove the trapped charge from the oxide. This bias dependence is shown in Fig. 10 for $T=125$ °C. With decreasing gate bias, the emission times become shorter, visible as a shift of the clusters to the left in the spectral maps. Particularly #3 and #6 show a very strong bias dependence. Also note the strong splitting in #4 and #6 (cf. Fig. 8). As has been shown before for the defects #4 and #6, electrostatic interaction is observed when defects lie in close vicinity of the same percolation path. During most experiments, where recovery is measured at the threshold voltage, the emission times of #6 are larger than #4, and consequently whenever #6 has captured a hole, it impacts the step height of the emission peak of #4. However, when the readout voltage is lowered, the emission times of #6 become shorter and #4 and #6 start to mutually influence each other in a much stronger manner. In particular, the average emission times of the subpeaks become different under these conditions.

IV. ANOMALOUS DEFECT BEHAVIOR

The spectral maps discussed so far basically correspond to what is expected from a two-state hole capture and emission process following multiphonon theory.[5,17,36] Interesting features such as the step-height splitting can be explained by simple electrostatic arguments. The same is true for a defect showing different average emission times for the two-step heights: due to the bias dependence of the emission time constant, a difference in the local potential around the defect will modify $\bar{\tau}_e$.

In addition to that, however, a number of peculiar details have been noticed which warrant further investigation. For instance, hole-capturing defects can disappear from the spectral map for random amounts of time. This is comparable to the phenomenon of anomalous RTN as has been observed for electron capture.[37]

As a first example, the metastability of defect #1 is shown in Fig. 11. Defect #1 is inasmuch interesting as its metastability went unnoticed for about half a year of measurements and analysis. While quickly scanning the recovery bias dependence of the emission time using short and optimized TDDS measurements, defect #1 became inactive for about three hours after which it resumed its regular activity.

In terms of its metastability, defect #7 is much more active and obvious: in the initial experiments at lower temperatures (≤150 °C), #7 appeared to behave like a regular defect with $\bar{\tau}_c \approx 50$ μs and $\bar{\tau}_e \approx 300$ s at 150 °C. At 175 °C, however, the defect stopped producing emission events for extended periods, even for stress times much larger than the previously extracted capture times. Following these extended periods of defect inactivity were periods with emission events recorded in nearly every trace. Also, after the end of the 175 °C experiment, #7 was inactive for a month during experiments at 125 °C before it reappeared. Apparently, this alternative metastable state of #7 is electrically neutral as it does not result in a threshold voltage shift. This is in contrast to the anomalous RTN defect recorded by Uren *et al.*,[37] which was able to capture an electron but stayed negatively charged in the alternative metastable state.

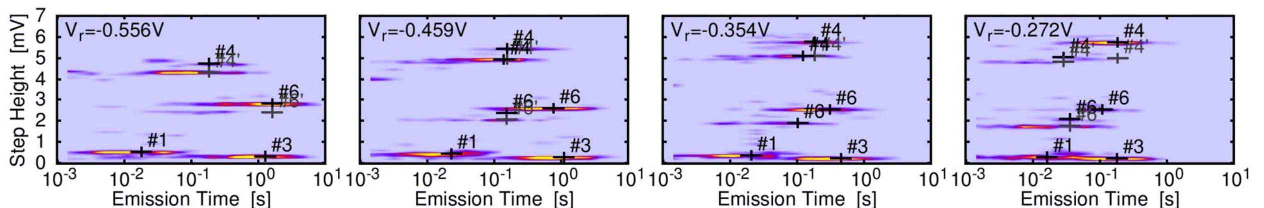

FIG. 10. (Color online) The recovery gate bias dependence of the spectral map at a temperature of 125 °C. With decreasing gate bias, the emission times become shorter, visible by a shift to the left of the clusters in the spectral maps. Particularly #3 and #6 show a very strong bias dependence. Also note the strong splitting in #4 and #6 (cf. Fig. 8). The subpeaks corresponding to the same defect may also have different emission times, visible in the above example for #4 and #6.

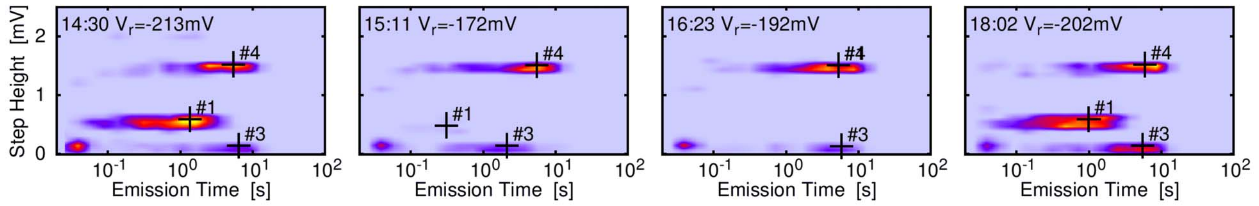

FIG. 11. (Color online) Metastability of defect #1 was briefly observed once while scanning $\bar{\tau}_e(V_r)$ at $T=75$ °C. During the measurement taken at 14:30 with $V_r=-213$ mV ($V_s=-1.7$ V, $T=75$ °C, and $t_s=10$ ms), defect #1 was 100% active. In the measurement started at 15:11 with $V_r=-172$ mV, #1 produced only three emission events and was completely inactive during the next measurement started at 16:23. #1 reappeared with $P_c \approx 1$ at 18:02.

Another intriguing feature was observed when the increase in the noise in the spectral maps with increasing stress time was inspected more closely. Even without additional defects appearing on the map, the number of errors encountered using the extraction of the approximation, Eq. (1), increased. Closer inspection revealed that in our particular device after a stress time of about 1 s, RTN appeared on a few traces, see Fig. 12. At a stress time of 10 s, the same RTN was present in nearly all traces. Quite intriguingly, during recovery the RTN disappeared after about a few milliseconds at 150 °C. We consequently suggest to term this phenomenon *temporary RTN*, or tRTN. The occurrence of this RTN was found to follow a stochastic process, similar to normal charge capture, that is, with increasing stress time and increasing T the number of traces showing tRTN increased. Also, the tRTN capture and emission times showed similar bias and temperature dependencies as the other defects. This phenomenon will be discussed in detail elsewhere.

V. EXTRACTED DEFECT PARAMETERS

To study the bias and temperature dependencies of the basic defect parameters we recorded more than 100 sets of spectral maps (with 5–8 maps per set) by more or less continuously measuring on a single device over a period of nine months. Within our range of voltages, temperatures, stress, and relaxation times, 13 defects could be identified on this device, corresponding to a reasonable defect density of 10^{11} cm^{-2}. The bias and voltage dependencies of the parameters of those defects which stayed within our experimental window and did not disappear could be studied over the whole operational regime of the transistor, starting from considerably below threshold up to voltages close to those used for oxide breakdown tests.

As an example, the extracted capture and emission time constants are shown in Figs. 13 and 14, which are clearly temperature activated with an activation energy of about 0.6 eV and depend in an nonexponential manner on the stress bias. A more detailed discussion of the bias and temperature dependencies of the capture and emission time constants together with a detailed nonradiative multiphonon model will be given in a subsequent publication.

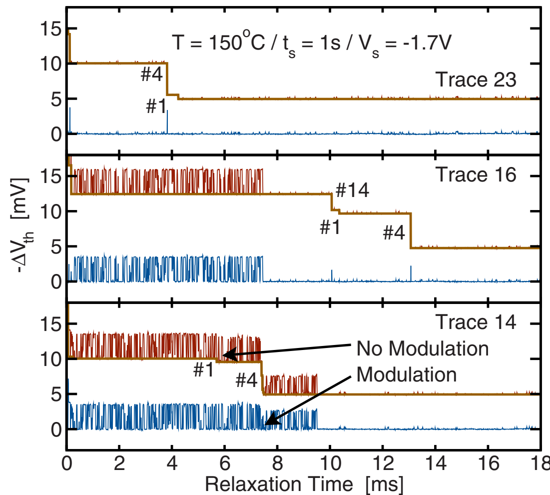

FIG. 12. (Color online) In addition to the discrete recovery steps, some traces contain temporary RTN, which disappear after about the average slow emission time, $\bar{\tau}_e^s$ of the defect. The extracted discrete steps are subtracted from the raw data to yield the noise trace. Just like with any other defect, the tRTN step height may be modulated by a change in another defect, in the above example, defect #4. By contrast, the emission event associated with #1 does not modulate the step height.

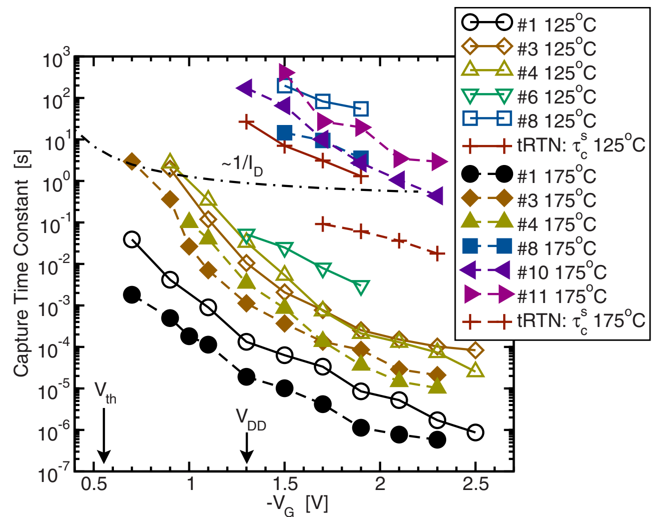

FIG. 13. (Color online) Voltage and temperature dependencies of the capture time constant for seven defects. Defect #6 was visible during the initial experiments only (taken at 125 °C) and then disappeared permanently, #10 and #11 were outside our experimental window at 125 °C. A strong-field/voltage dependence clearly different from exponential is observed for all defects. Also shown is the $1/I_D$ tendency expected from the standard SRH model (Ref. 5), which is considerably weaker.

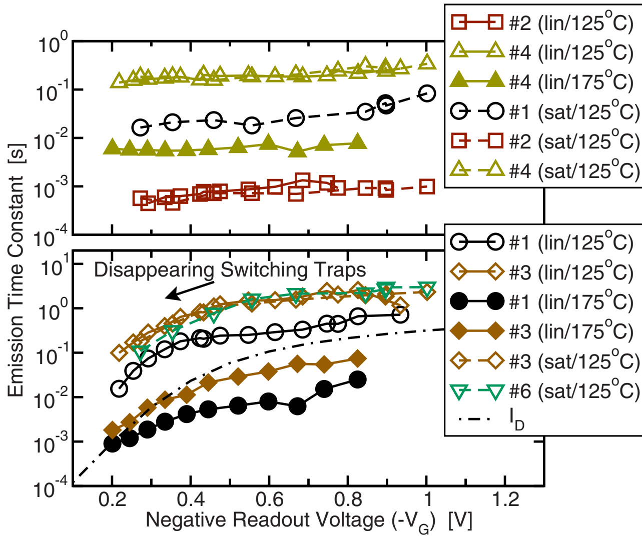

FIG. 14. (Color online) Gate voltage dependence of the emission time constant at 125 °C and 175 °C, measured in the linear and the saturation regime. Defects #1/sat, #2, and #4 (top) may be also described by a standard model as they only show a weak (if at all) field dependence at lower voltages. In contrast to that, $\bar{\tau}_e$ of defects #1/lin, #3, and #6 (bottom) show a pronounced V_G dependence at low bias. This behavior seems to coincide with the interfacial hole concentration, which is roughly proportional to I_D. Such a behavior cannot be explained with a standard model.

VI. DISCUSSION

The features of the TDDS can be summarized as follows: (1) the basic requirement to make a defect accessible by the TDDS is that its emission time constant falls within the experimental window. Typical time windows would be from the microsecond regime up to 100 or even 1 ks (covering about 7–9 decades in time), where the lower bound is determined by the measurement equipment while the upper bounds are mostly "limited by the experimenters patience."[17] Occasionally, a defect may have $\bar{\tau}_c$ outside the experimental window while $\bar{\tau}_e$ can be fully characterized. In our particular device this is the case for defects #2, #5, and #12, depending on the temperature and bias: due to the temperature dependence of the time constants, adjustment of the temperature allows to shift defects into the window. Similar considerations hold for $\bar{\tau}_c$, which can be brought into the window by appropriately selecting the stress voltage and temperature. (2) Even when more than a dozen defects contribute to the spectral map, each of them can be analyzed, provided that their characteristic times are separated by about a decade or the step height by more than about 0.5 mV (for the current device). For our device the latter can often be enforced by suitably adjusting the drain bias during recovery. For example, defects #1 and #3 have a step height of about 1 mV at $V_D=-1.2$ V. At $|V_G|<|V_{th}|$, the much stronger bias sensitivity of #3 results in a near overlap of the respective clusters on the spectral map. In contrast, at $V_D=-0.1$ V the step heights are 0.3 and 1.5 mV and no overlap of the clusters occurs. (3) The gate bias dependence of the capture time constant can be measured over nearly the whole operation range of the transistor, from slightly above threshold (in order to provide a sufficient probability of charging the fastest defects) up to oxide breakdown. Recall that the capture time constant is measured by comparing the occupation probability of the clusters on spectral maps recorded at different stress times around the capture time of defect. So even if $\bar{\tau}_c$ were inside the measurement window, $\bar{\tau}_c$ could not be characterized us-

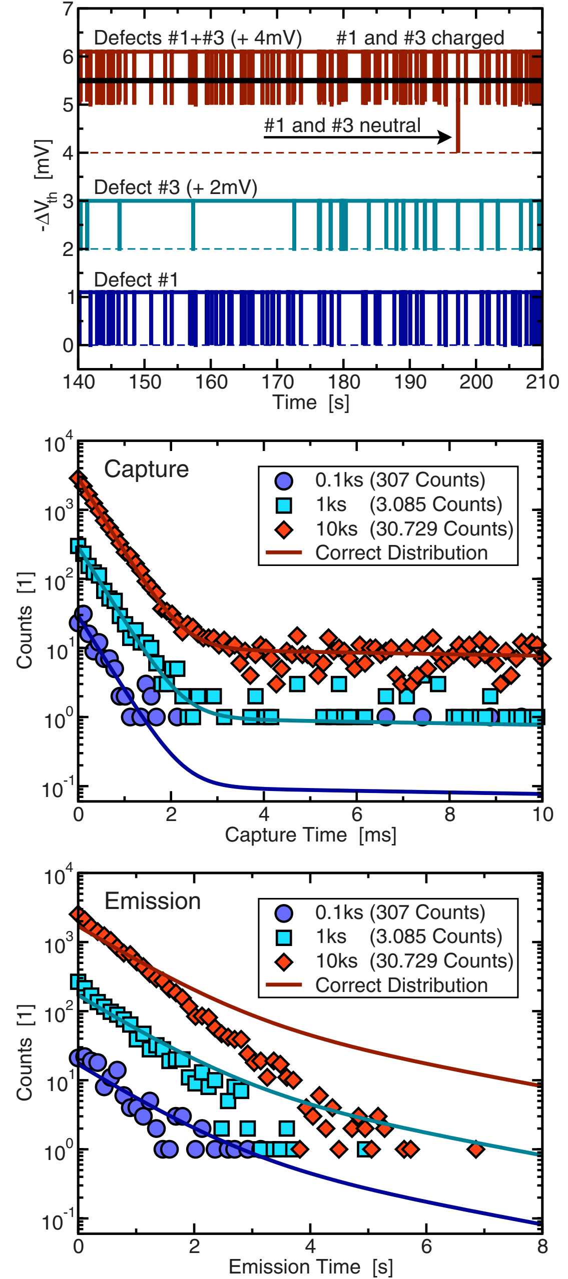

FIG. 15. (Color online) Simulated RTN at $V_G=V_D=-1.2$ V and 125 °C based on defects #1 and #3 only. Due to the widely different time constant but similar step heights, the overall RTN appears to be due to a single defect (top). A very large number of switching events needs to be analyzed to properly detect the nonexponential nature of the capture process (middle). However, the single-defect assumption indicated by the fat solid line at 5.5 mV in the top plot misses the superposition of the two exponential distributions and gives a wrong emission time constant (bottom).

ing the TDDS without $\bar{\tau}_e$ falling into the window as well. (4) The study of the gate bias dependence of the emission time constant is somewhat restricted since at low $|V_G|$ the minimum time constant obtainable with our measurement technique can increase significantly due to the small drain current. On the other hand, at high $|V_G|$, about 1 V in the present example technology, the drain current becomes too large to allow for a sufficiently accurate extraction of ΔV_{th}.

As a final example highlighting the strength of the TDDS, a simulated RTN of our sample device including only defects #1 and #3 is shown in Fig. 15. This case is interesting as at this bias condition both defects have similar step heights (1.1 and 1 mV) but widely different time constants ($\bar{\tau}_c^{(1)} \approx 0.4$ ms, $\bar{\tau}_e^{(1)} \approx 800$ ms, $\bar{\tau}_c^{(3)} \approx 40$ ms, and $\bar{\tau}_e^{(3)} \approx 2.8$ s). Since $\bar{\tau}_c \ll \bar{\tau}_e$ for both defects, they will be positively charged most of the time. As charge emission of these defects is uncorrelated, normally only one defect is briefly neutralized at a time. Thus, the probability of both defects becoming neutral at the same time is very small and the overall RTN may very likely pass as being due to a single defect (considering the overall noise level in a real experiment). Analysis of this RTN requires more than a thousand counts to reveal the contribution of two defects in the capture time constant. The situation is even worse for the emission time constant since the single-defect RTN analysis misses the nonexponential nature completely, resulting in a wrong emission time constant. Keeping in mind the extremely simplified situation with only two defects contributing to the RTN, it becomes clear that an RTN based on all 13 defects is virtually impossible to deconvolute. In contrast to that, analysis by the TDDS is exceptionally simple. For example, it is impossible to miss the fact that #1 and #3 are different defects, cf. Figs. 6–11.

VII. CONCLUSIONS

We have suggested the powerful TDDS for the analysis of border states. By recording the nonequilibrium response of a set of defects synchronized by a charging pulse and displaying them in a spectral map, the response of the defects is deconvoluted based on their capture times, emission times, and characteristic step heights, allowing for a relatively simple and straightforward analysis. In particular, when comparing this to the analysis of the random and uncorrelated contributions of a number of defects to a random-telegraph signal, the striking benefits of the TDDS become obvious: (i) analysis of the capture and emission time constants is possible over basically the complete operating regime of the transistor. (ii) Analysis of the capture time constant is possible up to oxide fields close to breakdown. (iii) Anomalous defect behavior in the form of disappearing defects and temporary RTN can be easily detected. (iv) Limitations on the measurement range are mostly due to the measurement resolution rather than by the occurrence of additional defects.

ACKNOWLEDGMENTS

The research leading to these results has received funding from the European Community's Seventh Framework Programme under grant Agreement No. 216436 (project ATHENIS) and the ENIAC project No. 820379 (MODERN). We also gratefully acknowledge stimulating discussions with W. Goes, F. Schanovsky, Th. Aichinger, Ph. Hehenberger, Ph. Roussel, D. Gillespie, M. Uren, and M. Kirton.

*grasser@iue.tuwien.ac.at

[1] B. Deal, IEEE Trans. Electron Devices **27**, 606 (1980).
[2] D. Fleetwood, IEEE Trans. Nucl. Sci. **39**, 269 (1992).
[3] P. Lenahan and J. Conley, Jr., J. Vac. Sci. Technol. B **16**, 2134 (1998).
[4] W. Shockley and W. Read, Phys. Rev. **87**, 835 (1952).
[5] M. Kirton and M. Uren, Adv. Phys. **38**, 367 (1989).
[6] D. Fleetwood, H. Xiong, Z.-Y. Lu, C. Nicklaw, J. Felix, R. Schrimpf, and S. Pantelides, IEEE Trans. Electron Devices **49**, 2674 (2002).
[7] J. Campbell, J. Qin, K. Cheung, L. Yu, J. Suehle, A. Oates, and K. Sheng, IEEE Int. Reliab. Phys. Symp. Proc. 382 (2009).
[8] T. Grasser, B. Kaczer, W. Goes, T. Aichinger, P. Hehenberger, and M. Nelhiebel, IEEE Int. Reliab. Phys. Symp. Proc. 33 (2009).
[9] D. Breed, Appl. Phys. Lett. **26**, 116 (1975).
[10] B. Kaczer, T. Grasser, J. Martin-Martinez, E. Simoen, M. Aoulaiche, P. Roussel, and G. Groeseneken, IEEE Int. Reliab. Phys. Symp. Proc. 55 (2009).
[11] T. Grasser and B. Kaczer, IEEE Trans. Electron Devices **56**, 1056 (2009).
[12] B. Kaczer, T. Grasser, P. Roussel, J. Franco, R. Degraeve, L. Ragnarsson, E. Simoen, G. Groeseneken, and H. Reisinger, IEEE Int. Reliab. Phys. Symp. Proc. 26 (2010).
[13] V. Huard, IEEE Int. Reliab. Phys. Symp. Proc. 33 (2010).
[14] J. Conley, Jr., P. Lenahan, A. Lelis, and T. Oldham, Appl. Phys. Lett. **67**, 2179 (1995).
[15] J. de Nijs, K. Druijf, V. Afanas'ev, E. van der Drift, and P. Balk, Appl. Phys. Lett. **65**, 2428 (1994).
[16] V. Afanas'ev and A. Stesmans, Europhys. Lett. **53**, 233 (2001).
[17] K. S. Ralls, W. J. Skocpol, L. D. Jackel, R. E. Howard, L. A. Fetter, R. W. Epworth, and D. M. Tennant, Phys. Rev. Lett. **52**, 228 (1984).
[18] S. Rauch, IEEE Trans. Device Mater. Reliab. **7**, 524 (2007).
[19] S. Machlup, J. Appl. Phys. **25**, 341 (1954).
[20] A. Karwath and M. Schulz, Appl. Phys. Lett. **52**, 634 (1988).
[21] A. Asenov, R. Balasubramaniam, A. Brown, and J. Davies, IEEE Trans. Electron Devices **50**, 839 (2003).
[22] E. Nicollian and J. Brews, *MOS (Metal Oxide Semiconductor) Physics and Technology* (Wiley, New York, 1982).
[23] H. Mueller and M. Schulz, J. Appl. Phys. **79**, 4178 (1996).
[24] T. Nagumo, K. Takeuchi, S. Yokogawa, K. Imai, and Y. Hayashi, Tech. Dig. - Int. Electron Devices Meet. 2009, 759.
[25] T. Grasser, H. Reisinger, W. Goes, T. Aichinger, P. Hehenberger, P. Wagner, M. Nelhiebel, J. Franco, and B. Kaczer, Tech. Dig. - Int. Electron Devices Meet. 2009, 729.

[26] H. Reisinger, T. Grasser, W. Gustin, and C. Schlünder, IEEE Int. Reliab. Phys. Symp. Proc. 7 (2010).
[27] D. Lang, J. Appl. Phys. **45**, 3023 (1974).
[28] J.-W. Chen, R. Ko, D. Brzezinski, L. Forbes, and C. Dell'oca, IEEE Trans. Electron Devices **28**, 299 (1981).
[29] D. Gillespie, *Markov Processes: An Introduction for Physical Scientists* (Academic Press, New York, 1992).
[30] D. Vuillaume, J. C. Bourgoin, and M. Lannoo, Phys. Rev. B **34**, 1171 (1986).
[31] D. Schroder and J. Babcock, J. Appl. Phys. **94**, 1 (2003).
[32] V. Huard, M. Denais, and C. Parthasarathy, Microelectron. Reliab. **46**, 1 (2006).
[33] T. Grasser, H. Reisinger, P.-J. Wagner, W. Goes, F. Schanovsky, and B. Kaczer, IEEE Int. Reliab. Phys. Symp. Proc. 16 (2010).
[34] H. Reisinger, O. Blank, W. Heinrigs, W. Gustin, and C. Schlünder, IEEE Trans. Device Mater. Reliab. **7**, 119 (2007).
[35] P. Kolev and M. Deen, J. Appl. Phys. **83**, 820 (1998).
[36] C. Henry and D. Lang, Phys. Rev. B **15**, 989 (1977).
[37] M. J. Uren, M. J. Kirton, and S. Collins, Phys. Rev. B **37**, 8346 (1988).